


# Crash 2 Squash: An Autonomous Drone for the Traversal of Narrow Passageways

## Journal Article

**Author(s):**

Fabris, Amedeo; Aucone, Emanuele; [Mintchev, Stefano](#) 

**Publication date:**

2022-11

**Permanent link:**

<https://doi.org/10.3929/ethz-b-000575022>

**Rights / license:**

[Creative Commons Attribution 4.0 International](#)

**Originally published in:**

Advanced Intelligent Systems 4(11), <https://doi.org/10.1002/aisy.202200113>

**Funding acknowledgement:**

186865 - CYbER - CanopY Exploration Robots (SNF)

# Crash 2 Squash: An Autonomous Drone for the Traversal of Narrow Passageways

Amedeo Fabris, Emanuele Aucone, and Stefano Mintchev\*

Access and exploration of confined and cluttered spaces is a major challenge in search and rescue, maintenance of infrastructures, and environmental monitoring. However, existing drones can only access passageways that are 30% narrower of their size. Herein, a drone that can squeeze its way through arbitrarily long passages that are half its width is presented. This is achieved by developing a quadrotor that synergistically embodies a soft foldable frame, multimodal mobility, and autonomous navigation. The drone exploits visual perception to detect the entrance of the gap and aerial mobility to align and fly toward it. The entry is made possible by the soft design of the frame, which passively folds without breaking when the drone flies and then collides at a controlled speed with the entrance of the passage, i.e., the “crash to squash” entry maneuver. Once inside, the quadrotor uses terrestrial locomotion for the traversal. The mechanical design of the drone and the performance of the “crash to squash” entry maneuver in passageways of different sizes are experimentally characterized. Finally, the control method is validated by indoor autonomous flights.

## 1. Introduction

Over the last two decades, aerial robots have gained exponential momentum, evolving from niche research platforms to essential instruments for various consumer and professional applications.<sup>[1]</sup> While drones have mastered flight in open environments for years, negotiating confined spaces with obstacles remains an open and timely research challenge.<sup>[2–7]</sup> Notably, the ability to access and traverse narrow passageways, crevices, and gaps would be advantageous for many applications such as search

and rescue,<sup>[8]</sup> inspection of ageing infrastructures,<sup>[9]</sup> and environmental monitoring.<sup>[10]</sup>


The complexity of exploring confined environments increases when the free space reduces relatively to the size of the drone. As this article investigates the traversal of horizontal passageways, we consider the gap-to-drone ratio  $\beta$  as a performance metric (Figure 1A,B). When  $\beta > 1$ , the environment contains sparse obstacles that can be detected and avoided.<sup>[3]</sup> Cages or other protective structures are added to drones to increase mechanical resilience when the likelihood of collisions increases as obstacles become more denser ( $\beta \approx 1$ ).<sup>[2,11]</sup> Eventually, to fly through gaps smaller than the width of the drone ( $\beta < 1$ ), an adaptive morphology is required whereby the drone folds to reduce its width (Figure 1D). Over the years, many morphing drones were specifically designed

for the task of gap traversal,<sup>[12–18]</sup> but the lack of multimodal mobility and a soft, collision-resilient body have limited their performance. When the drone folds into narrow passageways, the propellers move closer together. This reduces the arm of the force produced by each propeller and, consequently, the control torques available for maneuvering.<sup>[13]</sup> If the passage is very narrow, the propellers may even overlap. Their thrust is reduced, and so is their ability to support weight and maneuver.<sup>[19]</sup> Moreover, propellers generate turbulence when working near surfaces that can disturb or even hinder the stable flight of the drone.<sup>[20]</sup> Some morphing drones avoid flying inside passageways using a ballistic motion wherein the propellers are turned off, but this approach is only applicable to traverse short passageways.<sup>[12]</sup> Moreover, morphing drones are usually not designed to handle collisions, and often have exposed propellers that could hit the side walls of the passageway. Consequently, the size of the smallest traversable gap is increased by the addition of a safety factor on top of the width of the most compact configuration achievable by the morphing drone. An exception is the drone proposed by Patnaik et al.,<sup>[14]</sup> which uses passively folding propeller guards to slide along the walls of the passageway (Figure 1D) while approaching it at sustained speed. Furthermore, the traversal speed is reduced to trade off more stability at the expense of larger energy consumption and therefore length of the mission.<sup>[21]</sup> These are the main reasons why a gap-to-drone ratio of 0.7 is the current limit for morphing drones (Figure 1D).

Inspiration on how to lower this limit further can be sought in nature. The survival of animals often depends on their ability to

A. Fabris, E. Aucone, S. Mintchev  
Environmental Robotics Lab  
Swiss Federal Institute of Technology Zürich  
Universitätsstrasse 2, 8092 Zürich, Switzerland  
E-mail: stefano.mintchev@usys.ethz.ch

A. Fabris, E. Aucone, S. Mintchev  
Swiss Federal Institute for Forest, Snow and Landscape Research WSL  
Zürcherstrasse 111, 8903 Birmensdorf, Switzerland

 The ORCID identification number(s) for the author(s) of this article can be found under <https://doi.org/10.1002/aisy.202200113>.

© 2022 The Authors. Advanced Intelligent Systems published by Wiley-VCH GmbH. This is an open access article under the terms of the Creative Commons Attribution License, which permits use, distribution and reproduction in any medium, provided the original work is properly cited.

DOI: 10.1002/aisy.202200113

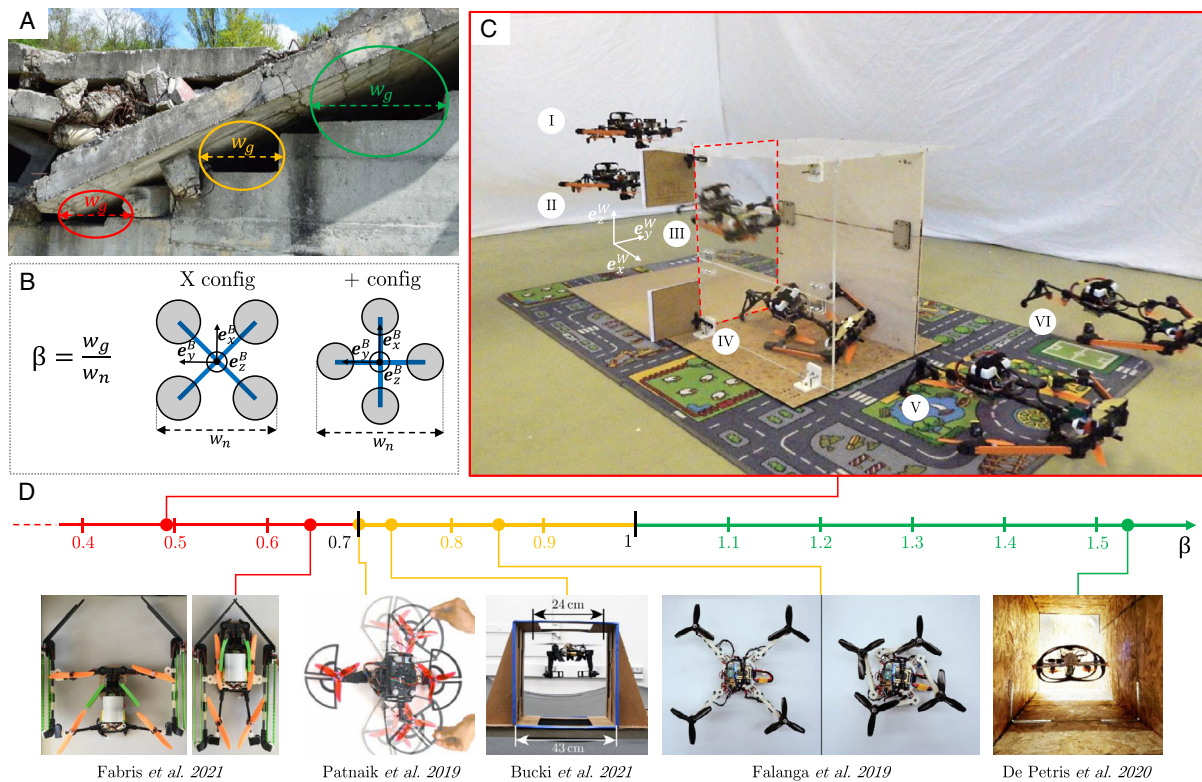


**Figure 1.** Traversing narrow and long passageways with drones. A) Examples of narrow gaps and passages of a partially collapsed building in a search and rescue scenario. B) Definition of the gap-to-drone ratio  $\beta$ :  $w_g$  represents the width of the gap and  $w_n$  is the nominal width of the drone during flight. C) The proposed drone traversing a narrow and long passageway: I) the drone autonomously aligns with the entrance of the passageway (highlighted by the dashed red contour); II) it approaches aiming at a controlled collision against the entrance of the passage; III) it squeezes on impact and IV) uses a series of wheels to crawl through the passageway; V) it detects the exit of the passageway; VI) it takes off again to continue its mission. D) Examples of state-of-the-art drones and their minimum  $\beta$ . The traversal is shown in Video S1, Supporting Information.

quickly traverse narrow gaps in dense vegetation to swoop down on a prey or flee an attack. These needs have seen insects and birds leverage their soft bodies<sup>[22]</sup> with streamlined shapes<sup>[23]</sup> to ease alignment and squeeze into tight spaces while surviving the inevitable collisions. These animals also fold their wings to reduce their size,<sup>[24,25]</sup> and use legs and claws to generate propulsion when flapping is precluded.<sup>[26]</sup> Soft morphing bodies and multimodal locomotion are combined with sharp perception and motion coordination into effective gap negotiation strategies.<sup>[27,28]</sup>

Some of these insights were successfully integrated by the authors into a morphing drone with multimodal mobility able to traverse gaps 65% of its nominal width.<sup>[29]</sup> However, this drone cannot access narrower passages because the reduction in frame width is limited, and manual flight makes alignment with the entrance of the passageway difficult and not repeatable.

In this article, we propose a gap-traversal drone with a completely redesigned soft foldable frame, multimodal mobility, and the perception and control capabilities for autonomous traversal of long and narrow passageways (Figure 1C). The drone exploits a controlled collision, which we refer to as “crash to squash,” to enter the passageway during flight. This method allows the access of suspended passageways that do not

necessarily have a landing spot in front of their entrance (e.g., Figure 1A). The controlled collision is made possible by the soft design of the frame, which passively squeezes without breaking when launched at controlled speed toward the entrance of the passageway. The traversal consists of six consecutive steps that build on the synergies between soft foldable frame, multimodal mobility, and autonomous navigation (Figure 1C). The drone detects the entrance of the gap, which is highlighted by four ArUco markers, and aligns itself with respect to it (step I), flies at sustained speed against the passageway (step II), leverages its momentum to fold the arms upon impact and squeeze inside the passageway (step III), activates the terrestrial locomotion to crawl through the confined space (step IV), and takes off again when the end of passageway is detected (step V and VI). With its novel mechanical design, the drone can reduce its width from 42 cm down to 17 cm enabling the traversal of even narrower passageways than<sup>[29]</sup> with different or changing shapes while ensuring more robustness to misalignments with respect to the entrance of the passageway.

In addition, the newly implemented flight autonomy increases the repeatability of successful entries especially for small passageways. Experiments prove the ability of the drone to traverse passageways down to 49% of the nominal width of the drone.

## 2. Implementation

In this section, we describe the implementation of the drone, focusing on both mechanical design and onboard computing. The drone is conceived to exploit the synergies between a soft foldable frame, multimodal mobility, and autonomy to enable traversal of narrow passages.

### 2.1. Mechanical Design

The proposed system is a quadrotor in plus configuration. The more traditional  $x$ -configuration used in the previous prototype<sup>[29]</sup> (Figure 1D) was abandoned to reduce the complexity of the design. Now, the width of the plus configuration can be reduced by folding two arms instead of four. Overall, such design simplification increases the folding ratio from 43% (in our previous work<sup>[29]</sup>) to 60% (in the presented design) and reduces the weight of the frame from 540 to 496 g (excluding the weight of the Intel RealSense T261 and the Khadas VIM3). The drone consists of (Figure 2): 1) a central T-shaped rigid structure; 2) a morphing system with two foldable arms; and 3) a terrestrial locomotion system.

The central part of the drone is made out of two carbon rods locked in a T-shaped structure by a 3D printed ABS connector (Figure 2). Additional connectors are inserted into this structure to accommodate the battery, two brushless (BLDC) motors for the front and rear propellers, the flight module consisting of flight controller (FC) and electronic speed controller (ESC), the companion computer required for autonomous navigation, and the bottom wheels for terrestrial locomotion. However, in the front, the drone hosts the stereo camera used for state

estimation and gap detection, and the mechanical connections to the foldable arms.

The morphing frame consists of two foldable arms implemented with carbon rods, each connected to the central T-shaped structure via a revolute joint. The two lateral motors and propellers are connected to the end of the arms via additional ABS connectors. The top view of the drone highlights how the folding arms create a streamlined arrow shape. This design feature is particularly important as it favors the passive alignment of the drone with the entrance of the passageway (Figure 2B). The arms fold passively and independently when the drone collides with the entrance of the passageway (step III in Figure 1C), allowing the transition from a nominal flight configuration to a folded configuration with reduced width (Figure 2B). For this reason, we reinforced with 3 mm-thick wooden lateral protections the external sides of the arms.

Passive folding, i.e., without the need for dedicated actuators, is another important design feature that reduces both mechanical complexity and weight. In addition, the absence of fragile actuators and mechanical transmission increases the resilience of the arms, thereby permitting the implementation of the “crash to squash” entry maneuver. The folding behavior of the arms is determined by two magnetic joints, one for each arm, and a tension spring (Figure 2C). The magnetic joints confer a dual-stiffness behavior to the arms,<sup>[30,31]</sup> i.e., they lock the arms in the nominal configuration providing the stiffness needed to fly in a stable and controlled manner, but disengage when the drone collides with the entrance to the passageway. The extension spring is connected via an inextensible wire (SpiderWire, 0.39 mm diameter, red line in Figure 2A) to a pulley coupled to each arm to resist the folding of the arms. This elastic

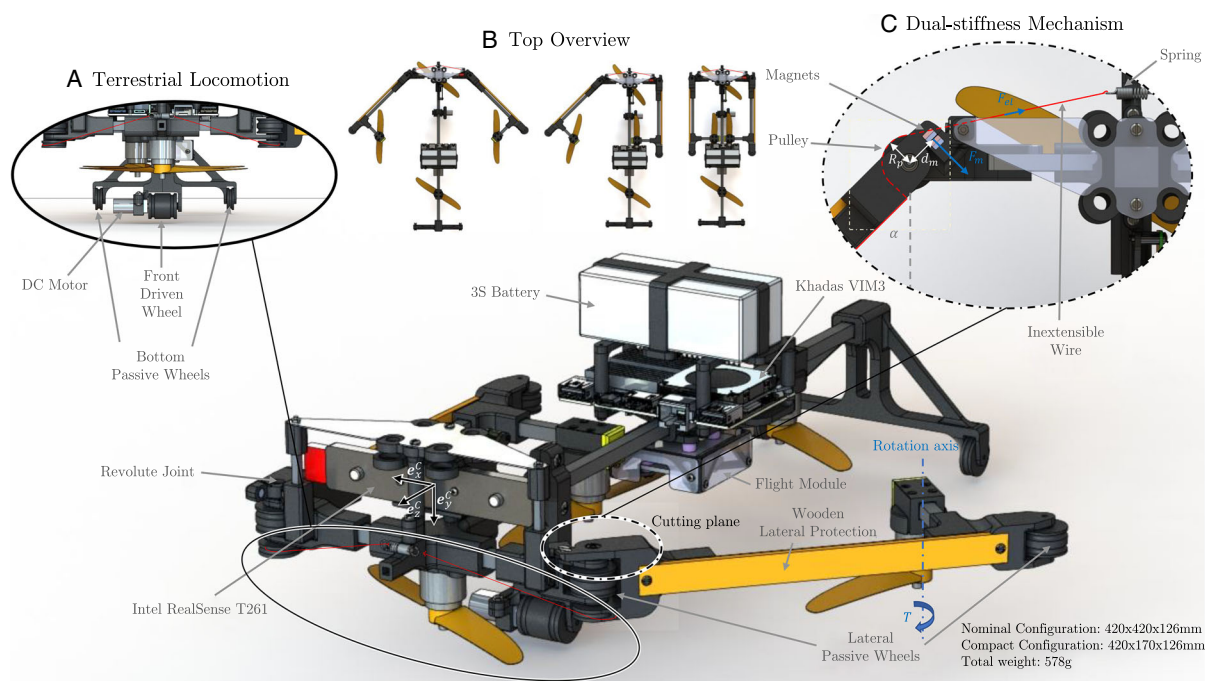


**Figure 2.** 3D model and general specifications of the drone. A) Front view of the terrestrial locomotion consisting of a front-driven wheel and two rear passive wheels; B) top view of the quadrotor in the nominal (left), partially folded (center), and compact (right) configurations; C) top sectional view of the dual-stiffness mechanism. At the bottom right corner of the image, the general characteristics of the drone are provided.



component confers a soft behavior to the arms once the magnet is disengaged, partially absorbs the energy of the impact during the entrance maneuver, and presses two lateral passive wheels against the sides of the passageway (Figure 1C). The spring also acts as a suspension in case of obstacles encountered during the navigation inside the passageway, as well as an eventual change of shape of the confined space. Moreover, the spring's exerted pressure allows the arms of the quadrotor to unfold once it exits from the passageway. To prevent propellers from colliding with the passageway walls and breaking, the brushless motors are offset from the drone arms with a short carbon rod half the length of the propeller. It is important to note that, as we stop the propellers before the collision, even if after the impact they are folded inward there is no risk of damaging any part of the drone or the blades themselves. In addition, the propellers are mounted in pusher configuration not only to improve efficiency in hover conditions,<sup>[32]</sup> but also to not interfere during folding with the electronics that is mounted on the top of the drone.

The drone uses terrestrial locomotion to avoid the aerodynamic and control challenges required to fly within narrow passageways. Terrestrial locomotion is achieved with a set of three wheels mounted on the bottom of the drone (Figure 2A). The front wheel is driven by a DC motor, while the two rear wheels are passive. These wheels are also exploited as landing gear for the drone. Additionally, two lateral passive wheels mounted at the extremities of the foldable arms allow to minimize friction with the walls of the passageways during crawling, and can also help to pull the drone inside the passageway or push it out at the exit.

## 2.2. Onboard Computing

The electronic payload of the quadrotor is tailored to the goal of autonomous gap traversal while maintaining a very lightweight configuration.

On the low level, the four brushless motors (BetaFPV 1506 3000KV coupled with 5030 two-blade propellers) are controlled by a Hobbywing XRotor Micro 4-in-1 40A ESC flashed with firmware that allows to braking the brushless motors on command. The ESC receives the desired rotor speed commands from a Radix LI flight controller on which a customized Betaflight firmware is flashed. The Radix LI can receive low-level commands from either the high-level controller running on the companion computer or a remote controller (RC) thanks to a FrSky XM + RC receiver via inverted SBUS signal.

The selected onboard computer is the Khadas VIM3 offering 4 A311D Cortex-A73 cores at 2.2 GHz paired with two Cortex-A53 cores at 1.8 GHz, alongside a Neural Processing Unit (5TOPS) and 4 GB of LPDDR4X RAM. It runs an Ubuntu 18.04 variant and ROS Melodic, and is responsible for all the sensor processing and the high-level control tasks onboard the drone. The drone integrates an Intel RealSense T261 tracker delivering visual-inertial odometry and working as a camera to detect the entrance of the passageway (see next section). The total weight of the sensing payload and the onboard computer is equal to 83 g. The Khadas VIM3 is powered by a 9 V/5 A Step-Down Voltage Regulator that is connected directly to the ESC, which is, in turn, powered by a SWAYTRONIC LiPo battery 3S 11.1 V 1000 mAh 6 °C/12 °C. The

stack of electronic boards is protected in the eventuality of collisions by sheets of 0.4 mm-thick fiberglass mounted on a 3D-printed ABS support.

The terrestrial locomotion is made possible by a brushed ESC connected on one end to the battery and on the other end to a DC motor (250:1 Micro Metal Gearmotor HP 6 V, Pololu, USA) that drives the bottom, frontal wheel of the drone.

## 3. Autonomous Gap Traversal Strategy

In this section, we analyze the gap traversal strategy with a focus on the synergies between mechanical design, perception, and control. As illustrated in Figure 3A, the strategy consists of six sequential steps.

First, the drone detects the gap and at the same time aligns itself with respect to the entrance of the passageways, which is highlighted by four ArUco markers (step I). Once the quadrotor is aligned, it executes the approaching trajectory to enter the passageway while continuously checking its proximity to the entrance of the confined space (step II). When the drone is closer than a given threshold to such entrance, the locomotion strategy is switched, i.e., the propellers are stopped and the DC motor for the terrestrial locomotion is activated (step III). At this stage, the drone collides thanks to its momentum with the entry of the confined space and passively folds to enter the passageway. This is what we call the “crash to squash” maneuver which solely relies on the mechanical design of the proposed drone. Then, the quadrotor navigates through the confined space by leveraging the terrestrial locomotion and the natural shape of the passageway to reach the exit (step IV). In the meantime, the accelerometer readings are monitored to detect the exit from the passageway (step V). Finally, the drone is outside of the passageway and switches back from terrestrial to aerial locomotion, by resetting the state estimate, which was corrupted during the collision, and takes off (step VI).

This strategy is coordinated according to the control system illustrated in Figure 3B. The autonomous intelligence is split into three main embedded systems, namely, the Radix LI, the Khadas VIM3, and the T261 (gray boxes in the figure). Each of these communicates with sensors and actuators (black boxes in the figure) by means of software modules (white boxes in the figure). The state estimate during the whole mission is provided by the Intel RealSense T261 tracking camera, whereas the onboard control logic and high-level tasks are implemented on the Khadas VIM3, and the low-level control is tackled by the RadixLI Flight Controller. To track the desired trajectories and to compute the thrust and body rates that are fed to the low-level controller which performs the body-rate-tracking and outputs, the desired single rotor thrusts needed for stabilization that gets then translated in motor commands. To this end, we employ the works of Faessler et al.<sup>[33,34]</sup> (the corresponding software modules are highlighted as high-level controller and low-level controller, respectively, in Figure 3A). In the following, the control algorithm for each step is described in more detail and the conditions that must be met before advancing to the next step are explained. These conditions are chosen such that the high-level controller can also satisfy them during the following steps. The duration of

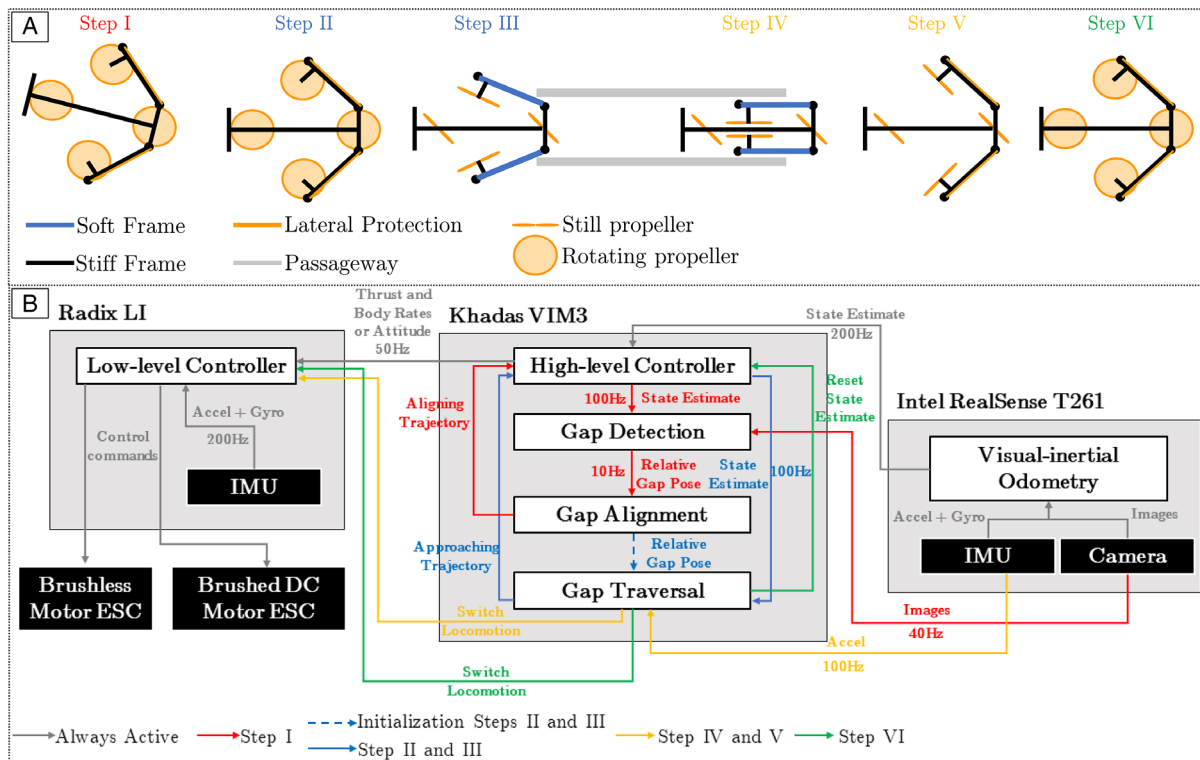


**Figure 3.** Strategy overview. A) Top view schematics of the adopted strategy. The proposed approach leverages autonomy combined with morphing capability, softness, and multimodal mobility simultaneously. B) Control system overview: the Radix LI and Khadas VIM3 communicate with each other over a UART interface, whereas this last one communicates with the T261 over USB 3.0. Black boxes are sensors and actuators; white boxes depict software modules. Color-coded arrows indicate the communications required by each step of the passageway traversal. Black arrows indicate communications that are always required throughout the whole autonomous navigation.

each step depends on how long it takes for the controller to meet the conditions and advance to the next step.

### 3.1. Gap Detection and Alignment

After taking off from the ground at point *W* (Figure 4), the drone hovers in front of the gap at point *A* and detects its entrance thanks to four squared ArUco markers<sup>[35]</sup> ( $0.107\text{ m} \times 0.107\text{ m}$ ,  $4 \times 4$  dictionary, one marker at each corner of the entrance of the passageway). The gap is detected in each image output at 40 Hz by the forward facing left fisheye camera of the stereo pair in the Intel RealSense T261. To speed up the computation, the gap is searched in a region of interest around the last detection. Only when no detection is found, the entire image is searched. The detection always follows the same sequence of steps: first, the image is undistorted and the ArUco Markers are detected;<sup>[35]</sup> then, as the metric size of the markers is known, the dimension of the gap and the 6-DOF pose ( $\mathbf{A}_{TAG}$  and  $\mathbf{R}_{AG}$  in Figure 4) of its center with respect to the drone coordinate frame is estimated by solving a Perspective-n-Points (PnP) problem. Let  $\Pi$  be the plane parallel to the entrance of the passageway and passing through its center *G*. Let  $\mathbf{e}_x^G$  and  $\mathbf{e}_y^G$  be the unit vectors spanning such plane  $\Pi$ , whose normal unit vector is  $\mathbf{e}_z^G$ . Thanks to the pose estimation of the gap, the gap alignment module computes the aligning trajectory in the world frame (Figure 4) in two steps:

- 1) an adjustment of the yaw  $\mathbf{B}\psi_G$  of the drone—at constant rate—in point *A*, to rotate the orientation of the drone to the plane  $\Pi$ ; 2) consequently, a motion parallel to the plane  $\Pi$ , while keeping the same distance from the entrance of the passageway (i.e.,  $\mathbf{B}\mathbf{r}_{AT}$ ), until it is completely (and frontally) aligned with the center of the gap (i.e., it reaches point *T* in Figure 4).

### 3.2. Approach and Entrance

When the drone hovers aligned with the center of the entrance of the passageway, the last detected relative pose of its center with respect to the drone is used to compute the ending point of the approaching trajectory in the inertial coordinate system. To force the drone to collide voluntarily against the entrance of the passageway, an artificial endpoint of the position of the gap is generated 1 m inside the passageway along the direction of  $\mathbf{T}\mathbf{r}_{TG}$ . In addition to this information and the yaw that the drone needs to maintain, also the real endpoint *G* is leveraged to understand the vicinity of the quadrotor with respect to the entrance of the gap. As the dimensions of the ArUco markers are known, also the width of the gap can be estimated and therefore a suitable approaching speed of the drone can be determined (see also Section 4.2 and Figure 5C). As a result, the drone flies toward the center of the artificial entrance of the passageway at the selected speed, continuously checking its distance with respect to the

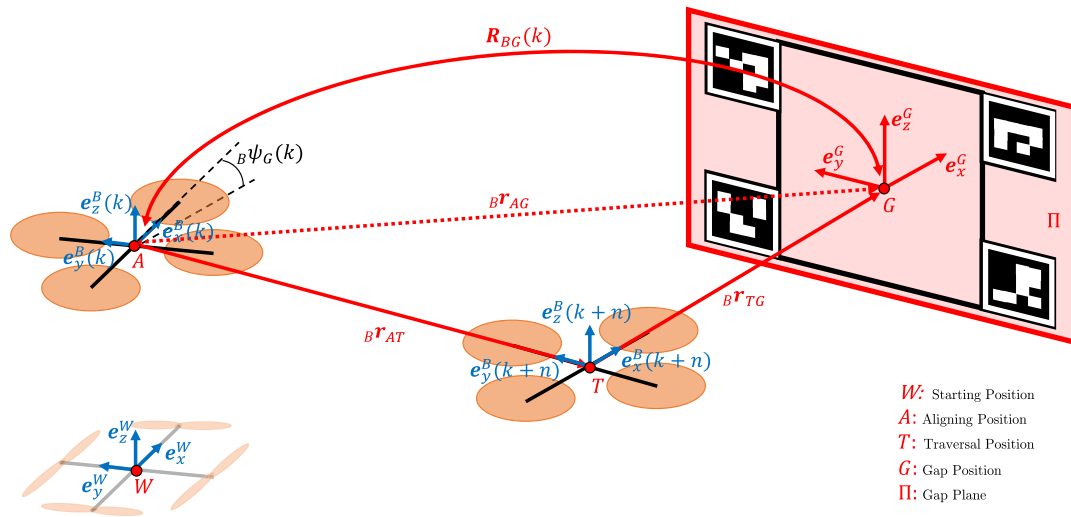


**Figure 4.** Overview of the coordinate system in the adopted control strategy.  $W$ : Starting point corresponding to the origin of the world frame  $W$  and the body frame  $B$  at time zero (i.e., at  $k = 0$ ), namely,  $[\mathbf{e}_x^B(0), \mathbf{e}_y^B(0), \mathbf{e}_z^B(0)] = [\mathbf{e}_x^W, \mathbf{e}_y^W, \mathbf{e}_z^W]$ .  $A$ : At time  $k$  the drone hovers at the aligning position  $A$  with a yaw offset  ${}_B\psi_G(k)$ , detects the gap, and aligns with it.  $T$ : At time  $k + n$  the drone have moved parallel to the plane  $\Pi$  to the traversal position  $T$ , and is aligned with respect to the center of the passageway  $G$  (i.e.,  ${}_B\psi_G(k + n) \approx 0$  and  ${}_B\mathbf{r}_{TG} \approx [{}_Bx_G, 0, 0]^T$ ).

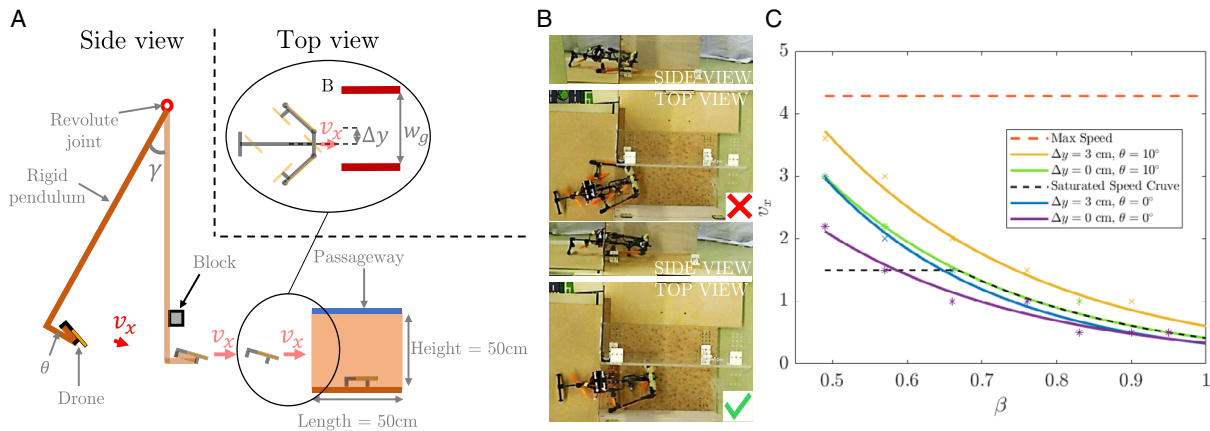


**Figure 5.** Results of the characterization. A) Schematic view of the pendulum tests displaying the definition of the variables of our experimental study. B) Examples of a successful (✓) or a failed (✗) entry maneuver. C) Plot showing the required minimum horizontal speed of the drone (y-axis) to access passageways with varying gap-to-drone ratio (x-axis): the red line represents the maximum tested speed; the yellow and green plots show the minimum required speed to traverse the passageways with pitch angle  $\theta = 10^\circ$  and  $\Delta y = 3$  cm and  $\Delta y = 0$  cm, whereas the blue and purple plots show the minimum required speed to traverse the passageways with a pitch angle  $\theta = 0^\circ$   $\Delta y = 3$  cm and  $\Delta y = 0$  cm, respectively.

actual position of such entrance. Up to this stage, the frame is in a rigid state to ensure stable and controlled flight (Figure 3B, step II). When a threshold of 5 cm is met, the drone is considered to be very close to the actual entrance of the passageway, as a consequence its propellers are stopped and the wheel for the terrestrial locomotion is activated. Thus, the drone collides with the entrance of the passageway (Figure 3B, step III). The forces experienced by the drone during this controlled collision cause the magnets to disengage and the frame to transition from a rigid to a soft state. The softening of the frame reduces the risk of damages during the collision. Due to the momentum induced by the sustained speed, the quadrotor is squeezed inside the passage. This is also facilitated by its streamlined shape, which also

compensates for any misalignment with the entrance of the passageway.

It is important to note that this collision will compromise the onboard state estimation of the platform, which will inevitably drift. Section 3.4 describes how this issue is addressed.

### 3.3. Terrestrial Locomotion and Exit

After entering, the quadrotor lands inside the passageway and its soft frame adapts to the size of the confined space. The terrestrial appendages are now in contact with both the lateral walls and the bottom of the passageway. Thus, the drone can crawl through the terrestrial locomotion, as shown in Figure 3B, step IV. During

the terrestrial locomotion, the drone checks the readings of the accelerometer of the camera module T261. Indeed, once the drone exits from the passageway, the spring allows the arms to recover their deployed configuration. The unfolding of the arms provokes a spike on the  $x$ -axis of the accelerometer on the camera ( $\mathbf{e}_x^C$  in the camera coordinate frame, Figure 2). To be robust to the noise of the sensor's readings, a moving median filter over a defined number of samples is performed. Hence, every time that the desired number of samples is collected, a median is computed among these samples, and the result is compared to a threshold that was determined experimentally. When this threshold is overcome, it means that the drone is outside the confined space and it has recovered its nominal configuration (Figure 3B, step V).

### 3.4. Takeoff

The drone is on the ground outside of the passageway and has a compromised state estimate consisting of a constant offset along  $\mathbf{e}_x^W$ ,  $\mathbf{e}_y^W$ , and  $\mathbf{e}_z^W$ . Therefore, the state estimate can be reset and shifted back to the origin by subtracting such constant offset (Figure 3B, step VI). Now the drone can take off and continue its mission.

## 4. Results

In this section, we characterize the drone with a series of measurements and experiments. We begin with the dimensioning the magnets of the foldable arms, then follow with the analysis of the main parameters impacting the success of the entry maneuver (i.e., gap width, horizontal speed, pitch angle, and misalignment), and finally report the results of the autonomous traversal tests.

### 4.1. Dimensioning of the Foldable Frame

The dual-stiffness behavior of the folding frame is controlled by the magnetic joint mounted in each arm which ensures the necessary stiffness of the airframe during flight (Figure 2C).

The magnets are selected to prevent the frame from folding during the flight due to the torque applied by the propellers on the arms. With reference to Figure 2C, this condition can be computed considering the rotational equilibrium of the arm

$$F_m d_m \geq T \quad (1)$$

where  $F_m$  is the holding force generated by the magnets,  $T$  is the torque of the propeller connected to the arm, and  $d_m$  is the distance between the center of the pulley and the center of the magnet. In the worst-case scenario, when  $T$  assumes the maximum value of 0.023 Nm, the magnets need to generate a holding force of at least  $F_m = 2.08$  N to prevent the folding of the frame. Therefore, we selected magnets producing a force of 5.2 N which ensures a safety factor of 2.5. When this threshold is exceeded, such as during a collision, the arms fold allowing the drone to squeeze inside the passageway.

### 4.2. Entry Maneuver

We call the entry maneuver "crash to squash" because it is a controlled collision wherein the drone uses its momentum to squeeze into the passageway (Figure 3, step III). In this section, we describe our study on the variables that have an impact during the entry maneuver of our strategy. The success of this highly dynamic maneuver is primarily influenced by the gap width ( $w_g$ ) and the drone's velocity at impact ( $v_x$ ), with pitch angle ( $\theta$ ) and lateral misalignment with respect to the entry ( $\Delta y$ ) also playing an important role. Due to the dynamics of a quadrotor, speed and pitch angles are intertwined as the drone needs to pitch in order to move forward. Therefore, these two variables cannot be decoupled during steady forward flight unless the drone is equipped with some tiltable rotors.<sup>[36]</sup> To decouple these two variables, and study the effect of the others, we simulated the flight of the drone by launching it using a pendulum (Figure 5A). The drone is accelerated during the descent and is released and launched toward the entrance of the passage when the pendulum hits a stop block. We tested passageways of seven different widths (corresponding to  $\beta = 0.91, 0.87, 0.80, 0.73, 0.64, 0.55, 0.49$ ). To have a statistical estimation of the successful entrance of the drone inside the passageway, each experiment is repeated three times. The entry maneuver is considered successful if the drone can engage the bottom-driven wheels and the lateral passive wheels on the floor and walls of the passageway, respectively (see Figure 5B), in at least two launches out of three.

#### 4.2.1. Horizontal Speed and Pitch Angles

To select  $v_x$ , the starting position of the pendulum is set at different inclinations  $\gamma$ . We tested various horizontal speeds of the drone ranging from 0.5 to 4.3 m s<sup>-1</sup> (namely, we tested  $v_x = 0.5, 1, 1.5, 2, 2.2, 3, 3.6, 4.3$  m s<sup>-1</sup>). The pendulum is equipped with an adjustable end to launch the quadrotor with different pitch angles  $\theta$  ranging from 0° to 30° with increments of 10°.

A quick round of drone launches against various passages showed that the probability of successful entry decreases significantly for  $\theta \geq 20^\circ$ . In this condition, the impact forces during the entry maneuver are not entirely transmitted along the morphable direction of the drone, hampering significantly its entry maneuver. In addition, at high horizontal speed ( $v_x \geq 2$  m s<sup>-1</sup>), the drone could flip making it impossible for the drone to recover. The performance increases significantly with lower pitch angles  $\theta \leq 10^\circ$ .

#### 4.2.2. Misalignment

We tested lateral misalignments up to 3 cm which is the maximum value allowed by the narrowest passageway. This geometric constraint is imposed by the mechanical design of the proposed drone. Indeed, the T-shaped structure imposes a flat rigid head in front of the system as wide as the propeller. If the passageway is narrow (close to the diameter of the propeller), small misalignments could cause the drone to hit the side of the passageway with this flat rigid part making it impossible for the drone to change its shape, and therefore access the confined space.



#### 4.2.3. Discussion

Figure 5C summarizes the results of our experimental study by showing the minimum speeds required by the drone in succeeding to enter inside each of the seven passageways without misalignment and with pitch angle  $\theta = 0^\circ$  and  $\theta = 10^\circ$  (blue and yellow plots, respectively), and with a 3 cm misalignment and pitch angle  $\theta = 0^\circ$  and  $\theta = 10^\circ$  (purple and green plots, respectively). The red dashed line marks the maximum tested speed. In general, the range of possible velocities to succeed in entering the passageways decreases from the largest passageway to the narrowest one with an increasing pitch angle. Narrower passageways require higher speeds ( $v_x \geq 1.5 \text{ m s}^{-1}$ ) as the drone needs to fold more to enter the passageway successfully (Figure 5C). Moreover, as expected, the drone requires more speed and therefore an increased momentum for misaligned entries. In this scenario, each arm of the quadrotor gets folded independently and in two subsequent impacts. A first impact would happen between one of the arms of the drone and a single wall of the passageway. This single point of impact acts as a pivoting contact forcing the drone to rotate around the yaw axis and lose speed in the direction of the passageway. During this rotation, the other unfolded arm of the quadrotor would collide with the second wall of the passageway decreasing further the momentum of the platform. Overall, the drone proves to have a high tolerance to lateral misalignment (up to 3 cm) as it can access all the tested passageways with the correct approaching speed. Finally, if we consider only the launches executed for low pitch angles (i.e.,  $\theta \leq 10^\circ$ ), the drone was able to enter successfully inside a given passageway with a success rate of 85% for all the tested velocities.

#### 4.3. Autonomous Gap Traversal

The quadrotor has been deployed in the same passageways as for the pendulum experiments to test the autonomous gap traversal. Moreover, we deployed the drone in two additional scenarios to test its ability to access and to traverse suspended long pipes (having therefore circular entrance), and passageways with varying shape. A video demonstrating the traversals of these passages with different dimensions is provided in the Supporting Information.

##### 4.3.1. Analysis

Figure 6 shows the traversal of a passageway with  $\beta = 0.55$ . The figure provides an overview of the position of the drone over time according to its states, and snapshots of the drone during the maneuver. During the alignment, the drone changes its pose with respect to the gap until it is aligned (i.e., until  ${}_B Y_G \approx 0 \text{ cm}$ ,  ${}_B Z_G \approx 0 \text{ cm}$ , and  ${}_B \psi_G \approx 0^\circ$  in Figure 6, step I). At this point, the drone is in the approaching phase. Hence, it moves closer to the gap while maintaining the same height (i.e.,  ${}_W x_B$  progressively increases and  ${}_W z_B$  remains constant in Figure 6, step II). The entrance is detected and logged very quickly (cf., Figure 6, step III, represented by the green dot and the solid line), and after the collision the estimated position in the world drifts. Now, the drone switches to the terrestrial

locomotion strategy and navigates into the passageway. At this stage, although its estimated pose had drifted, the position of the gap with respect to the drone ( ${}_B Y_G$ ,  ${}_B Z_G$ , and  ${}_B \psi_G$  in step IV of Figure 6) remains not updated. Finally, the drone detects the exit (step V) and after 3 s resets the state estimate (i.e.,  ${}_W x_B$  and  ${}_W z_B$  go back to zero in Figure 6, step VI) and the drone can take off and continue its mission.

##### 4.3.2. Discussion

Three autonomous flights were performed for each of the seven widths of the passageway. Table 1 gives an overview of the results obtained during these tests. The third column of Table 1 highlights the success rate of the drone in entering the passageways during three autonomous flights. The last column shows the estimated speed of the drone along the traversable direction of the passageway averaged over all the tests which led to a successful entrance. Overall, the system had entered all the passageways. Passageways, having a width between 38.5 and 30.8 cm, were always entered successfully, whereas the success rate of narrower passageways decreases with the dimension of the passageway (i.e., with  $\beta \leq 0.55$ ). In this scenario, the drone requires horizontal speed  $v_x \geq 2 \text{ m s}^{-1}$  to successfully enter the passageway (as predicted by the pendulum tests in Figure 5C). Moreover, the drone was also able to successfully access a long suspended pipe, traverse passageways of varying shapes (last two rows of Table 1), and even enter narrower passageways from the ground (i.e., leveraging only the terrestrial locomotion) corresponding to a  $\beta = 0.45$  (all these experiments are shown in the Video S1, Supporting Information). The drone not only showed robustness to misalignments that occurred in estimation errors of the pose of the gap, but also mechanical resilience as it never broke during all the experiments except for some lateral propellers in the early stage of the deployment.

##### 4.3.3. Limitations

During the tests, the maximum speed has been saturated at  $v_x = 1.5 \text{ m s}^{-1}$  (black dashed line in Figure 5C) and the maximum run-up distance (i.e., the initial distance between the gap and the drone) has been limited to at most 1 m. There are two reasons for this. First, the pose of the gap with respect to the drone is estimated with onboard vision during the alignment step. Once this step is concluded, the drone is accelerated toward the entrance and its alignment is no longer corrected. Therefore, even small alignment errors around the yaw axis (e.g.,  $1^\circ$ ) lead to large lateral misalignments if the drone is far away from the entrance of the passageway. Second, such a short distance would force the drone to increase the pitch angle considerably ( $\theta \geq 20^\circ$ ) to reach high speeds ( $v_x > 1.5 \text{ m s}^{-1}$ ), but this would compromise the entry maneuver. In future iterations, a longer run-up distance can be achieved by increasing alignment accuracy or by periodically realigning the drone while approaching. In the case of a short run-up distance, which is common in confined environments, the drone would need to perform a more complex approach maneuver initiated with a rapid acceleration at a high pitch angle to achieve high speed followed by a pitch correction to level the drone just before entering.

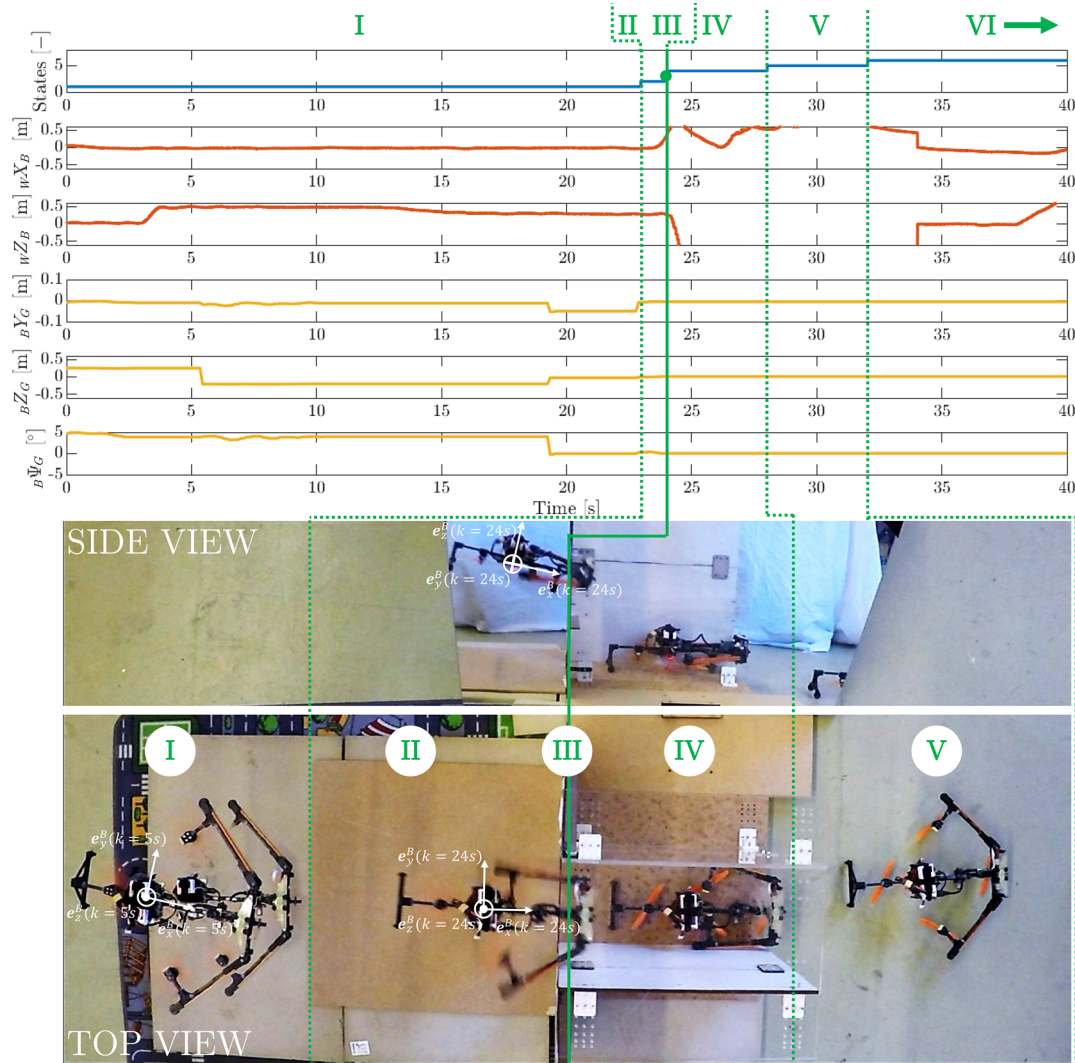


**Figure 6.** Example of autonomous gap traversal. The top image contains the plots showing the log data during one of the several deployments. Blue lines show the various states of the drone (i.e., the steps of the control strategy). Red lines illustrate the position of the drone in world frame. Yellow lines express the pose of the gap with respect to the drone (i.e., in body frame). The bottom image displays the side and the top view sequences of a successful entrance in the passageway having  $\beta = 0.55$ . The experiment is filmed from above and the additional side view is possible thanks to an inclined mirror.

**Table 1.** Summary of the results of the deployment.

Deployment overview					
Height [cm]	Length [cm]	$w_g$ [cm]	$\beta$	Success rate [%]	$v_{x_{avg}}$ [m s <sup>-1</sup> ]
50	50	20.7	0.49	33	1.5
50	50	23.1	0.55	33	1.45
50	50	27.1	0.64	66	$1.4 \pm 0.03$
50	50	30.8	0.73	100	$1.1 \pm 0.06$
50	50	34	0.80	100	$0.9 \pm 0.05$
50	50	36.6	0.87	100	$0.86 \pm 0.04$
50	50	38.5	0.91	100	$0.7 \pm 0.05$
35.1	100	35.1	0.83	66	$1.0 \pm 0.05$
35.1	150	35.1	0.83	66	$1.0 \pm 0.05$

## 5. Conclusions

We presented a drone that uses a “crash to squash” strategy to traverse narrow passageways 51% smaller than its size. This strategy leverages the synergies between autonomous navigation, a soft, foldable frame, and multimodal mobility to enable the drone to fly, squeeze, and crawl through narrow passages. Autonomous navigation guarantees precision and repeatability in approaching the entrance of the passageway. The foldability of the frame confers to the drone the softness required to safely squeeze between the walls of the passageway by simply flying against it, i.e., without the need for additional actuators. Finally, the additional terrestrial mobility enables crawling in confined spaces where propellers would not have enough space to rotate. Overall, the drone can access the passageways, even when misaligned, with a pitch angle  $\theta \leq 10$  and with a speed

ranging from  $0.7\text{ ms}^{-1}$  up to  $1.5\text{ ms}^{-1}$ . To the best of the authors' knowledge, this is the first drone to achieve the goal of traversing passageways that are half its size ( $\beta = 0.49$ ).

In the next steps, we will refine the drone to improve its performance. As far as perception is concerned, although the presented drone can already access confined spaces with different shapes, the entrance of such spaces needs always to be highlighted by four ArUco markers because they guarantee a precise and repeatable estimation of the drone's pose relative to the entrance of the passageway with low computing power. A valid alternative to cope with real-world gaps at the cost of more computing power (GPUs) would be to use temporally stacked spatial parallax or TS<sup>2</sup>P.<sup>[37]</sup> The use of tiltable rotors (e.g., ref. [36]) would provide the high speed needed to access narrow passages without a long running start or high pitch angles. Use in real-world scenarios will require exiting passageways that are not at ground level. We anticipate that the drone could be equipped with the necessary propulsion to burst out of the passage, deploy, and recover stable flight thanks to state-of-the-art control algorithms such as ref. [38]. Furthermore, although we have shown that simple wheels are sufficient to traverse narrow passages, real-world scenarios will require more robust and reliable locomotion mechanisms to ensure robustness over rough and complex terrain (e.g., wheels<sup>[39]</sup> or tracks<sup>[29]</sup>). Finally, the curious reader may wonder when "small is too small." We believe that the "crash to squash" strategy remains valid for narrower passageways (i.e.,  $\beta < 0.5$ ), but its implementation will require even softer drones with continuously deformable frames that stretch and flex. This will be possible by bridging the gap between soft and aerial robotics enabling new design and control paradigms for soft drones.

## Supporting Information

Supporting Information is available from the Wiley Online Library or from the author.

## Acknowledgements

The research was supported by the Swiss Center for Drones and Robotics of the Department of Defence, Civil Protection and Sport via armasuisse S+T under project number 050-42, by the ETH Zurich Research Grants, and by the SNSF Eccellenza grant number 186865.

## Conflict of Interest

The authors declare no conflict of interest.

## Data Availability Statement

Data available on request from the authors.

## Keywords

aerial robotics, foldable mechanisms, multimodal mobility, soft robotics

Received: May 4, 2022

Revised: July 28, 2022

Published online: September 23, 2022

- [1] D. Floreano, R. J. Wood, *Nature* **2015**, 521, 460.
- [2] A. Briod, P. Kornatowski, J.-C. Zufferey, D. Floreano, *J. Field Robot.* **2014**, 31, 496.
- [3] A. Loquercio, E. Kaufmann, R. Ranftl, M. Müller, V. Koltun, D. Scaramuzza, *Sci. Robot.* **2021**, 6, eabg5810.
- [4] D. Falanga, K. Kleber, D. Scaramuzza, *Sci. Robot.* **2020**, 5, eaaz9712.
- [5] Y. Mulgaonkar, A. Makineni, L. Guerrero-Bonilla, V. Kumar, *IEEE Robot. Autom. Lett.* **2017**, 3, 596.
- [6] B. Landry, R. Deits, P. R. Florence, R. Tedrake, in *2016 IEEE International Conference on Robotics and Automation (ICRA)* **2016**, 1469–1475, <https://doi.org/10.1109/ICRA.2016.7487282>.
- [7] R. Allen, M. Pavone, in *AIAA Guidance, Navigation, and Control Conf.*, AIAA, Reston, Virginia, USA **2016**, p. 1374.
- [8] J. Delmerico, S. Mintchev, A. Giusti, B. Gromov, K. Melo, T. Horvat, C. Cadena, M. Hutter, A. Ijspeert, D. Floreano, L. M. Gambardella, R. Siegwart, D. Scaramuzza, *J. Field Robot.* **2019**, 36, 1171.
- [9] D. Lattanzi, G. Miller, *J. Infrastruct. Syst.* **2017**, 23, 04017004.
- [10] C. H. Cannon, C. Borchetta, D. L. Anderson, G. Arellano, M. Barker, G. Charron, J. M. LaMontagne, J. H. Richards, E. Abercrombie, L. F. Banin, et al., *Front. For. Glob. Change* **2021**, 160.
- [11] P. De Petris, H. Nguyen, T. Dang, F. Mascari, K. Alexis, in *IEEE Int. Symp. on Safety, Security, and Rescue Robotics*, IEEE, Piscataway, NJ **2020**, pp. 84–89.
- [12] V. Riviere, A. Manecy, S. Viollet, *Soft Robot.* **2018**, 5, 541.
- [13] D. Falanga, K. Kleber, S. Mintchev, D. Floreano, D. Scaramuzza, *IEEE Robot. Autom. Lett.* **2018**, 4, 209.
- [14] K. Patnaik, S. Mishra, S. M. R. Sorkhabadi, W. Zhang, in *IEEE/RSJ Int. Conf. on Intelligent Robots and Systems*, IEEE, Piscataway, NJ **2020**, pp. 1364–1370.
- [15] N. Bucki, J. Tang, M. W. Mueller, arXiv preprint arXiv:2103.16632, **2021**.
- [16] N. Bucki, M. W. Mueller, in *Int. Conf. on Robotics and Automation*, IEEE, Piscataway, NJ **2019**, pp. 9116–9122.
- [17] M. Zhao, T. Anzai, F. Shi, X. Chen, K. Okada, M. Inaba, *IEEE Robot. Autom. Lett.* **2018**, 3, 1176.
- [18] K. Patnaik, W. Zhang, *Int. J. Intell. Robot. Appl.* **2021**, 5, 365.
- [19] A. Fabris, K. Kleber, D. Falanga, D. Scaramuzza, in *IEEE Int. Conf. on Robotics and Automation*, IEEE, Piscataway, NJ **2021**, pp. 592–598.
- [20] P. Sanchez-Cuevas, G. Heredia, A. Ollero, *Int. J. Aerosp. Eng.* **2017**, 2017 1823056.
- [21] L. Bauersfeld, D. Scaramuzza, *IEEE Robot. Autom. Lett.* **2022**, 7, 2953.
- [22] K. Jayaram, R. J. Full, *Proc. Natl. Acad. Sci. USA* **2016**, 113, E950.
- [23] C. Li, A. O. Pullin, D. W. Haldane, H. K. Lam, R. S. Fearing, R. J. Full, *Bioinspir. Biomimet.* **2015**, 10, 046003.
- [24] C. D. Williams, A. A. Biewener, *Proc. Natl. Acad. Sci. USA* **2015**, 112, 3392.
- [25] P. Henningsson, *Roy. Soc. Open Sci.* **2021**, 8, 211072.
- [26] K. Saito, R. Pérez-De La Fuente, K. Arimoto, Y. Seong, H. Aonuma, R. Niiyama, Z. You, *Proc. Natl. Acad. Sci. USA* **2020**, 117, 17622.
- [27] I. G. Ros, P. S. Bhagavatula, H.-T. Lin, A. A. Biewener, *Interface Focus* **2017**, 7, 20160093.
- [28] I. Schiffner, H. D. Vo, P. S. Bhagavatula, M. V. Srinivasan, *Front. Zool.* **2014**, 11, 1.
- [29] A. Fabris, S. Kirchgeorg, S. Mintchev, in *IEEE Int. Symp. on Safety, Security, and Rescue Robotics*, IEEE, Piscataway, NJ **2021**, pp. 48–54.
- [30] S. Mintchev, S. de Rivaz, D. Floreano, *IEEE Robot. Autom. Lett.* **2017**, 2, 1248.
- [31] S. Mintchev, J. Shintake, D. Floreano, *Sci. Robot.* **2018**, 3, eaau0275.

- [32] B. Theys, G. Dimitriadis, P. Hendrick, J. De Schutter, in *Int. Conf. on Unmanned Aircraft Systems*, IEEE, Piscataway, NJ **2016** pp. 195–201.
- [33] M. Faessler, A. Franchi, D. Scaramuzza, *IEEE Robot. Autom. Lett.* **2018**, 3, 620.
- [34] M. Faessler, D. Falanga, D. Scaramuzza, *IEEE Robot. Autom. Lett.* **2016**, 2, 476.
- [35] S. Garrido-Jurado, R. Muñoz-Salinas, F. J. Madrid-Cuevas, M. J. Marn-Jiménez, *Pattern Recog.* **2014**, 47, 2280.
- [36] P. Zheng, X. Tan, B. B. Kocer, E. Yang, M. Kovac, *IEEE Robot. Autom. Lett.* **2020**, 5, 6845.
- [37] N. J. Sanket, C. D. Singh, K. Ganguly, C. Fermüller, Y. Aloimonos, *IEEE Robot. Autom. Lett.* **2018**, 3, 2799.
- [38] M. Faessler, F. Fontana, C. Forster, D. Scaramuzza, in *IEEE Int. Conf. on Robotics and Automation*, IEEE, Piscataway, NJ **2015**, pp. 1722–1729.
- [39] S. Mintchev, D. Floreano, in *Proc. of the 2nd Int. Symp. on Aerial Robotics*, **2018**, <https://infoscience.epfl.ch/record/255681?ln=en>.